









# Two Homologous Quasi-periodic Fast-mode Propagating Wave Trains Induced by Two Small-scale Filament Eruptions

Jincheng Wang<sup>1,2,3</sup> , Xiaoli Yan<sup>1,2,3</sup> , Zhike Xue<sup>1,2</sup> , Liheng Yang<sup>1,2</sup> , Qiaoling Li<sup>4</sup> , Zhe Xu<sup>1,3</sup> , Liping Yang<sup>1,5</sup>, and Yang Peng<sup>1,5</sup>

<sup>1</sup> Yunnan Observatories, Chinese Academy of Sciences, Kunming 650011, People's Republic of China; [wangjincheng@ynao.ac.cn](mailto:wangjincheng@ynao.ac.cn)

<sup>2</sup> Yunnan Key Laboratory of Solar Physics and Space Science, Kunming 650011, People's Republic of China

<sup>3</sup> Center for Astronomical Mega-Science, Chinese Academy of Sciences, 20A Datun Road, Chaoyang District, Beijing, 100012, People's Republic of China

<sup>4</sup> Department of Physics, Yunnan University, Kunming 650091, People's Republic of China

<sup>5</sup> University of Chinese Academy of Sciences, Yuquan Road, Shijingshan Block Beijing 100049, People's Republic of China

Received 2022 July 4; revised 2022 August 15; accepted 2022 August 18; published 2022 September 2

## Abstract

We present two homologous quasi-periodic fast-mode propagating (QFP) wave trains excited by two small-scale filament eruptions nearby a sunspot on 2017 September 12. By using observations from several ground-based and space-based instruments, it is found that the eruptions of two small-scale filaments resulted in some accompanying solar phenomena/activities (such as radio bursts, GOES C-class flares, coronal bright fronts, and QFP wave trains). The QFP wave trains run behind the main coronal bright fronts with a constant propagating speed of about  $800 \text{ km s}^{-1}$ , while two main coronal bright fronts traveled away from the flare kernel obeying the power-law functions of  $S(t) = 894.9 * (t - 7.43)^{0.60} + 76.8$  and  $S(t) = 705.3 * (t - 19.12)^{0.47} + 57.5$ , respectively. The period of the first QFP wave train was estimated to be about 59 s, while the second QFP wave train has two periods of about 70 and 37 s. On the other hand, the intensity peaks of 94 and 335 Å passbands in the flare kernel exhibit some perturbations during the occurrences of the QFP wave trains. With the wavelet analysis and their synchronization, these perturbations and the QFP wave trains are tightly related phenomena, which suggests that they have a common exciting mechanism. Furthermore, we find that the emissions of the intensity peak mainly originate from the one footpoint of flare loops during the occurrence of the QFP wave trains. According to the above features, we conclude that the QFP wave trains are excited in the energy release process associated with magnetic reconnection and are closely related to the outflow of the magnetic reconnection.

*Unified Astronomy Thesaurus concepts:* [Solar coronal waves \(1995\)](#); [Solar atmosphere \(1477\)](#); [Solar filament eruptions \(1981\)](#)

*Supporting material:* animations

## 1. Introduction

Solar flares/coronal mass ejections (CMEs) are the main manifestations of solar storms, which are considered to be caused by the impulsive release of nonpotential energy through magnetic reconnection (e.g., Antiochos et al. 1999; Lin & Forbes 2000; Xue et al. 2016; Yan et al. 2018, 2022). They are closely correlated with filament eruptions and solar jets (Munro et al. 1979; Yokoyama & Shibata 1995; Gilbert et al. 2000; Schmieder et al. 2015; Wang et al. 2017; Li & Yao 2020). However, the exact triggering mechanisms of solar flares/CMEs are not fully understood. On one hand, these violently energetic releases will have a significant influence on the solar atmosphere, resulting in various solar phenomena/activities (e.g., coronal dimming, Reinard & Biesecker 2008; rearrangements of the magnetic field, Xu et al. 2019; turbulence in the chromosphere or corona, Warmuth 2015; sunspot reversal rotation, Bi et al. 2016). On the other hand, they also will inevitably excite various types of magnetohydrodynamic (MHD) waves that may evolve into different shock waves (Nakariakov & Verwichte 2005; Takasao & Shibata 2016; Li et al. 2020).

Chromospheric Moreton–Ramsey waves and coronal bright fronts (CBFs)/extreme-ultraviolet (EUV) waves are flare-associated phenomena (Moreton 1960; Moreton & Ramsey 1960). Either or both of them would be discovered in various flare events, which propagate outward from the epicenter with an arch-shaped front (Cabezas et al. 2019; Wang et al. 2020). Moreton–Ramsey waves are proposed as enhancement signatures when a coronal fast-mode magnetosonic wave or shock sweeps the chromosphere (Uchida 1968), while CBFs are interpreted as the real coronal fast-mode magnetosonic shock waves (Ofman & Thompson 2002) or the plasma compression due to successive stretching or opening of closed field lines during the flare (Chen et al. 2002). Wang et al. (2020) studied an event in which a small-scale filament eruption excited a Moreton and an EUV wave and suggested that Moreton and different passband EUV waves are the perturbations in different temperature-associated layers induced by a coronal MHD shock wave. Type II radio bursts, generated by the electron acceleration in coronal shocks, a good indicator of coronal shocks, often can be discovered during some wave events (e.g., Reiner et al. 2007; Kozarev et al. 2011; Duan et al.

2022). Many authors show that CBFs have a stronger association with CMEs than flares (Biesecker et al. 2002; Nitta et al. 2013; Muhr et al. 2014). The properties of these large-scale MHD waves could be utilized to diagnose various important physical parameters, which is a useful method to



Original content from this work may be used under the terms of the [Creative Commons Attribution 4.0 licence](#). Any further distribution of this work must maintain attribution to the author(s) and the title of the work, journal citation and DOI.

estimate the magnetic field strength in the corona (Liu & Ofman 2014).

Coronal quasi-periodic fast-mode propagating (QFP) wave trains, first discovered by Liu et al. (2010, 2011) with the unprecedented image observations of the 171 Å passband from the Solar Dynamics Observatory (SDO), are composed of multiple, coherent, arc-shaped wave fronts with propagating speeds of  $\sim 500\text{--}2000\text{ km s}^{-1}$  (Shen et al. 2022). The periods of QFP range from dozens of seconds up to a few minutes (Shen et al. 2022), which are comparable to that of the flare quasi-periodic pulsations (QPPs; e.g., Tan et al. 2010; Ning 2014; Li et al. 2021; Ning et al. 2022). They can run ahead of or behind the CME bubble (Liu et al. 2012) and can also be excited by a solar jet event (Duan et al. 2022). So far, the excitation mechanism of these phenomena is still controversial. Some authors suggest that QFPs are generated by the intermittent pulses of energy release associated with the intermittent magnetic reconnection in a flare kernel (Liu et al. 2010, 2011; Shen & Liu 2012; Miao et al. 2021; Zhou et al. 2021). By performing a set of two-dimensional MHD simulations, Takasao & Shibata (2016) found that the QFPs can be spontaneously excited by the local oscillation in the flare kernel. However, some people proposed that the dispersion of fast broad propagating magnetosonic waves caused by some waveguide structures (such as coronal loop, fibrils, and magnetic separatrix in the corona) also could result in the generation of QFPs in the corona (Pascoe et al. 2013; Yuan et al. 2013; Nisticò et al. 2014). Therefore, more observational clues are needed to figure out the exact excitation mechanism of QFPs.

In this letter, we report two homologous QFP wave trains induced by the homologous eruptions of two small-scale filaments near a sunspot on 2017 September 12. Analyzing the characteristics of two homologous QFP wave trains, we also discuss and probe the generation mechanism of QFP wave trains. The sections of this letter are organized as follows: observations and data reductions are described in Section 2, main analysis results are presented in Section 3, and the summary and discussions are given in Section 4.

## 2. Observations and Data Reductions

Two homologous QFP wave trains of interest occurred in NOAA Active Region 12680 during two small-scale filament eruptions at around 07:20 UT and 19:01 UT on 2017 September 12. The two events were captured by instruments from the New Vacuum Solar Telescope<sup>6</sup> (NVST; Liu et al. 2014; Yan et al. 2020), the Atmospheric Imaging Assembly (AIA; Lemen et al. 2012) on board SDO<sup>7</sup> (Pesnell et al. 2012), and the Global Oscillation Network Group<sup>8</sup> (GONG; Harvey et al. 1996). NVST can provide high-resolution image observations of the H $\alpha$  band with an 11 s cadence and a spatial resolution of  $0''.165\text{ pixel}^{-1}$ . AIA can provide seven simultaneous full-disk EUV images of the low corona and transition region with a pixel spatial size of  $0''.6$  and a cadence of 12 s. We mainly utilize the image observations of 193, 335, and 94 Å EUV passbands in our study. H $\alpha$  image observations with 1-minute cadence and a spatial resolution of  $1''\text{ pixel}^{-1}$  from GONG instruments are also utilized to demonstrate the

filament eruption. To reduce the effect of the Sun's rotation and differential rotation, the AIA and GONG images were derotated to a reference time of 07:30 UT for the first event and a reference time of 19:00 UT for the second event. In addition, the soft X-ray flux data from the Geostationary Operational Environmental Satellite-13<sup>9</sup> (GOES-13), the radio observation from the WAVES instrument (Bougeret et al. 1995) on the Wind<sup>10</sup> spacecraft, and line-of-sight (LOS) magnetic field from the Helioseismic and Magnetic Imager (HMI; Hoeksema et al. 2014) on board SDO are also utilized in this study.

## 3. Results

### 3.1. Two Small-scale Filament Eruptions

The first event of interest, in which a small-scale filament erupted beside a sunspot, occurred in NOAA AR 12680 (N09E41) during the period from 07:18 UT to 07:45 UT on 2017 September 12. Figures 1(a1)–(a4) show the process of the filament eruption in NVST H $\alpha$  observations. At 07:18 UT, a filament with some chromospheric fibers resided at the southwest of the sunspot. The filament generally lifted and separated from some chromospheric fibers at around 07:23 UT, and then some chromospheric brightenings also spread around the filament. Eventually, the filament erupted entirely at around 07:33 UT (see panel (a4)). The eruption coincided with a GOES C3.0 flare and a radio burst. The flare started at 07:22 UT, peaked at 07:27 UT, and ended at around 07:34 UT (see the blue and red lines in the inset of panel (b2)). A main fast frequency-drifting type III emission in radio emission, extending from more than 10 MHz to 100 kHz, was detected by Wind/WAVES during the small-scale filament eruption (see the inset in panel (b2)).

Some coronal perturbations propagating away from the source region could be discerned in SDO/AIA EUV observations. The signatures of these perturbations are more pronounced in the 193 and 211 Å channels than other channels. Panels (b1)–(b2) of Figure 1 show the 193 Å images during the eruption, while panels (c1)–(c2) are the 193 Å running-difference images. Some arch-shaped bright fronts, traveling behind the main CBF, could be distinguished in the 193 Å running-difference observations (see panels (c1)–(c2) and the animation of Figure 1), which are marked by the black arrow in panels (c1)–(c2). They traveled in the same direction as the main CBF and emanated successively near the epicenter of the accompanying flare. This feature could be identified as the signal of a QFP wave train (Shen et al. 2022).

The second event of interest, similar to the first one, in which a similar small-scale filament erupted, occurred at the same location about 12 hr later during the period from 18:57 UT to 19:35 UT. Figures 2(a1)–(a4) show the eruption process of the filament in GONG H $\alpha$  observations. At around 18:57 UT, a dark filament resided at the same place as the first one (see panel (a1)). At around 19:08 UT, this filament began to erupt. Some material in the northern part of the filament lifted, and some brightenings appeared and expanded generally (see panels (a2)–(a3)). Eventually, this filament erupted entirely at around 19:19 UT (see panel (a4)). Like the first event, this filament eruption also induced a GOES C1.6 flare and a radio

<sup>6</sup> <http://fso.ynao.ac.cn>

<sup>7</sup> <https://sdo.gsfc.nasa.gov>

<sup>8</sup> <https://gong.nso.edu>

<sup>9</sup> <https://www.goes.noaa.gov>

<sup>10</sup> <https://solar-radio.gsfc.nasa.gov/wind/index.html>

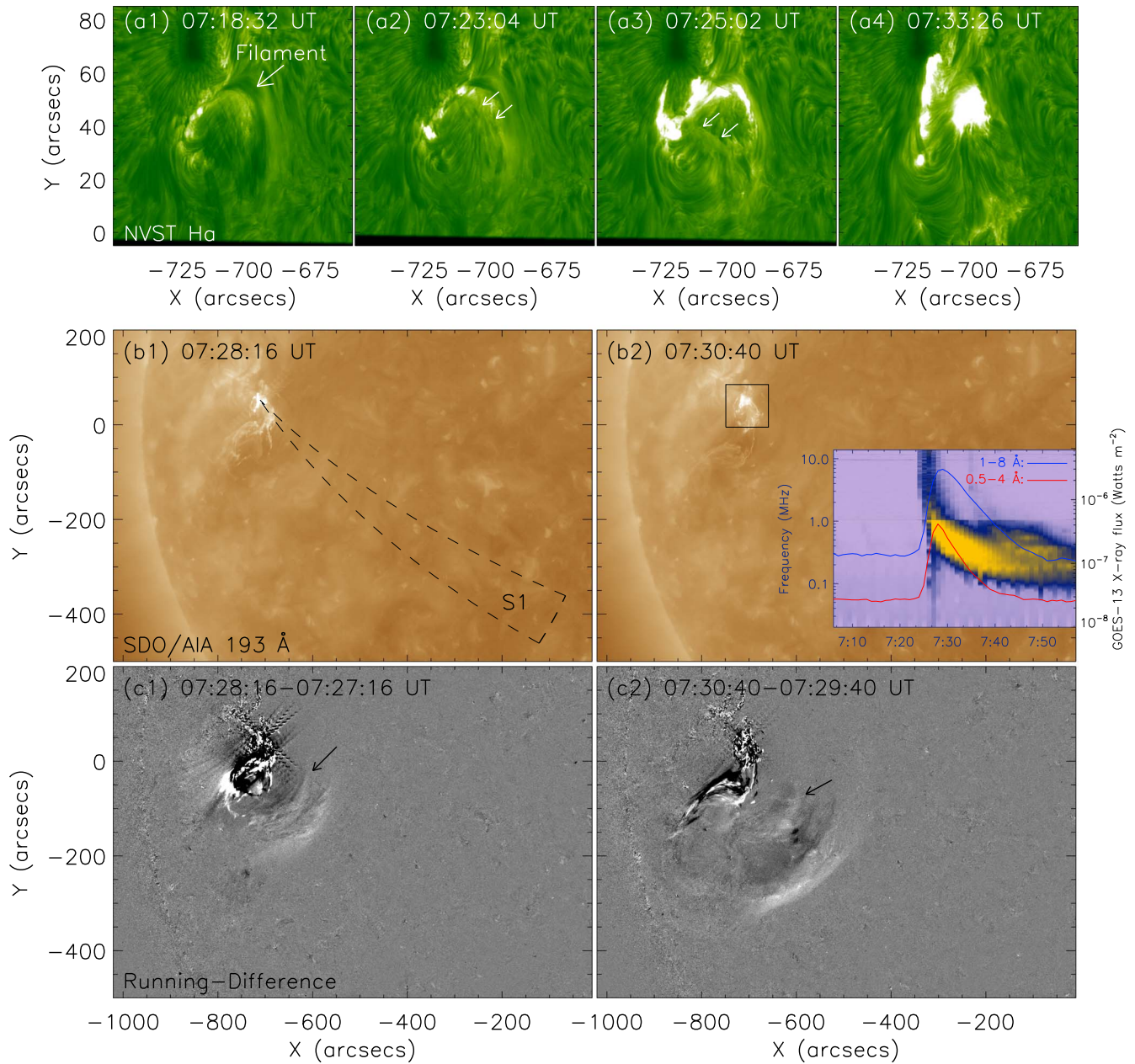


**Figure 1.** Observations of the first event. (a1–a4) NVST H $\alpha$  images. The white arrows mark the small-scale filament. (b1–b2) SDO/AIA 193  $\text{\AA}$  maps. The black dashed line S1 in panel (b1) outlines the path for restructuring the time–distance map of Figures 3(a) and (b). The black box in panel (b2) outlines the region of panels (a1)–(a4). The inset in panel (b2) represents the radio emission from Wind/WAVES as the background, overlaid by the GOES soft X-ray fluxes of 0.5–4  $\text{\AA}$  (red line) and 1–8  $\text{\AA}$  (blue line). (c1–c2) Running-difference maps of SDO/AIA 193  $\text{\AA}$ . An animation of panels (b1) and (c1) is available. The animation shows the propagation of the first QFP wave train during the period from 07:18 UT to 07:38 UT. The animation duration is 4 s.

(An animation of this figure is available.)

burst (see the inset in panel (b2) of Figure 2). The flare started at 19:03 UT, peaked at 19:20, and ended at 19:28 UT. There is a bulge in the soft X-ray flux profiles of 0.5–4  $\text{\AA}$  and 1–8  $\text{\AA}$  at around 19:08 UT. A frequency-drifting emission in radio emission, extending from more than 5 MHz to 20 kHz, was captured by Wind/WAVES during the period from 19:08 UT to 19:20 UT (see the inset in panel (b2)).

By using the observations of SDO/AIA, some coronal perturbations could also be discerned during the eruption. The main CBF, marked by blue arrows, first runs away from the eruption region (see Figures 2(c1)–(c2)). Then, some arch-shaped bright fronts, appearing at the place marked by the

black arrow, could also be identified behind the main CBF (see panels (c1)–(c2) and the animation of Figure 2). They also emanated successively near the epicenter of the accompanying flare. We identify them as the signal of the QFP wave train.

### 3.2. The Characteristics of CBFs and QFP Wave Trains

To quantify the kinematics of the main CBFs and QFP wave trains in two events, we restructured time–distance maps by using the intensity profile technique (Liu et al. 2010; Wang et al. 2020). Figure 3(a) shows the time–distance maps restructured by 193  $\text{\AA}$  running-difference images along the sector of S1 in Figure 1(b1) for the first event, while Figure 3(c)



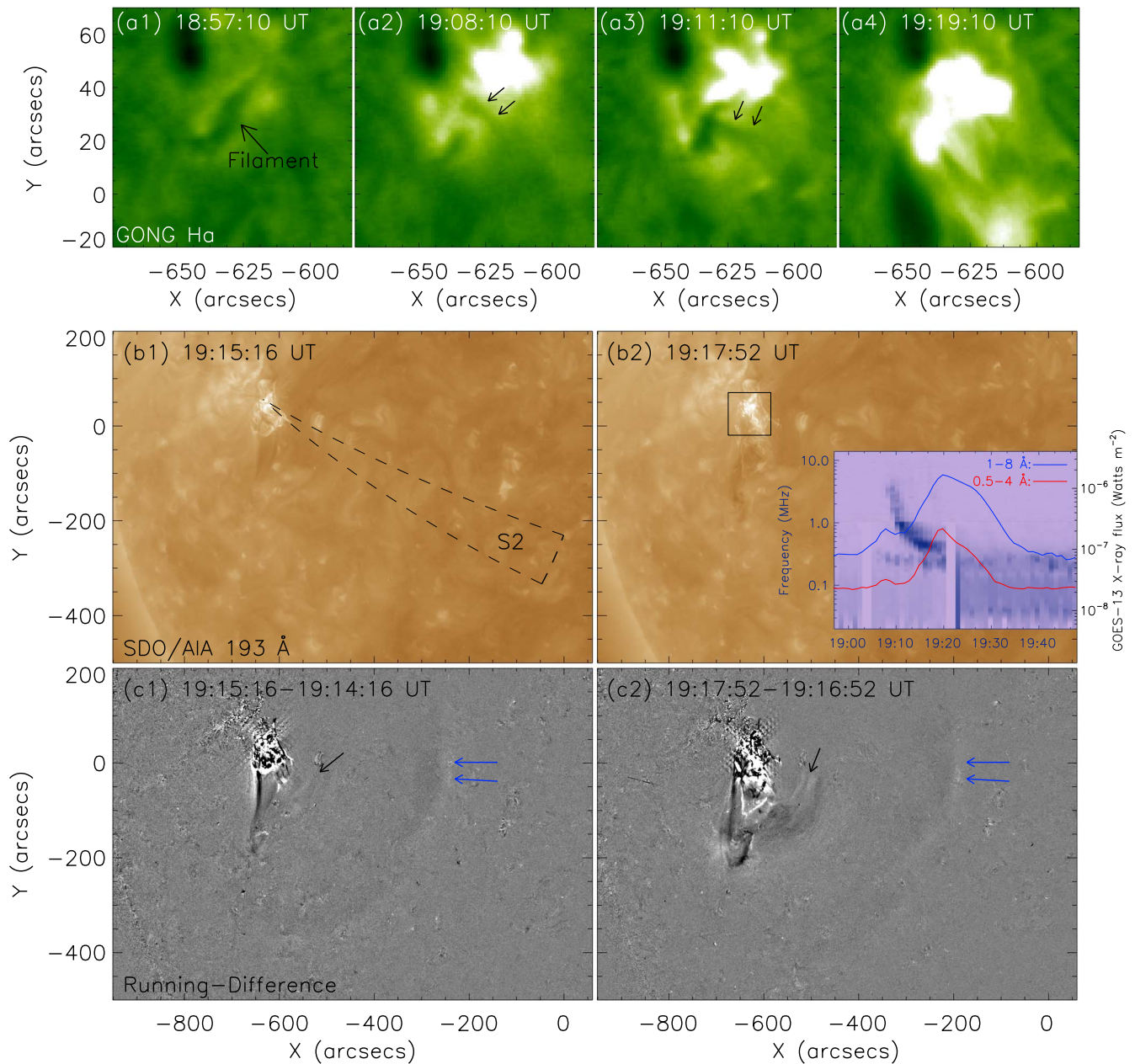


**Figure 2.** Same as Figure 1, but for the second event. (a1–a4) GONG  $H\alpha$  images. The black arrows mark the small-scale filament. (b1–b2) SDO/AIA 193  $\text{\AA}$  maps. The black dashed line S2 in panel (b1) outlines the path for restructuring the time–distance map of Figure 3(c) and (d). The black box in panel (b2) outlines the region of panels (a1)–(a4). The inset in panel (b2) represents the radio emission from Wind/WAVES, overlaid by the GOES soft X-ray fluxes of 0.5–4  $\text{\AA}$  (red line) and 1–8  $\text{\AA}$  (blue line). (c1–c2) Running-difference maps of SDO/AIA 193  $\text{\AA}$ . An animation of panels (b1) and (c1) is available. The animation shows the propagation of the second QFP wave train during the period from 19:00 UT to 19:32 UT. The animation duration is 6 s.

(An animation of this figure is available.)

is the time–distance map along the sector of S2 in Figure 2(b2) for the second event. The propagation trajectories of different waves could be highlighted by the different stripes in the time–distance maps. We find that the main CBFs of two events traveled on the solar surface with a power-law function, which is consistent with the previous study (Wang et al. 2020). This fact demonstrates that the main CBFs are the freely propagating shock waves (Warmuth & Mann 2011). We use a power-law function to fit their propagation distances ( $S$ ) with time ( $t$ ), to obtain that they follow the functions of  $S(t) = 894.9 * (t - 7.43)^{0.60} + 76.8$  and  $S(t) = 705.3 * (t - 19.12)^{0.47} + 57.5$ , respectively.

On the other hand, some aligned stripes occurred after the main EUV waves, which are marked by the black arrows in panels (a) and (c). They are considered as the signals of QFP wave trains in the time–distance maps. The first appearance of the QFP wave train was about 100 Mm from the flare kernel, and the propagation distances of the QFP wave trains could up to about 150 Mm. Panels (b) and (d) are the zoom-in regions of QFP signals marked by the yellow boxes in panels (a) and (c). For the first QFP wave train, four wave fronts could be tracked with visual inspection, marked by the white lines in panel (b). Based on their slope and interval, we could obtain that its propagating speed was about  $815 \pm 58 \text{ km s}^{-1}$  and its period

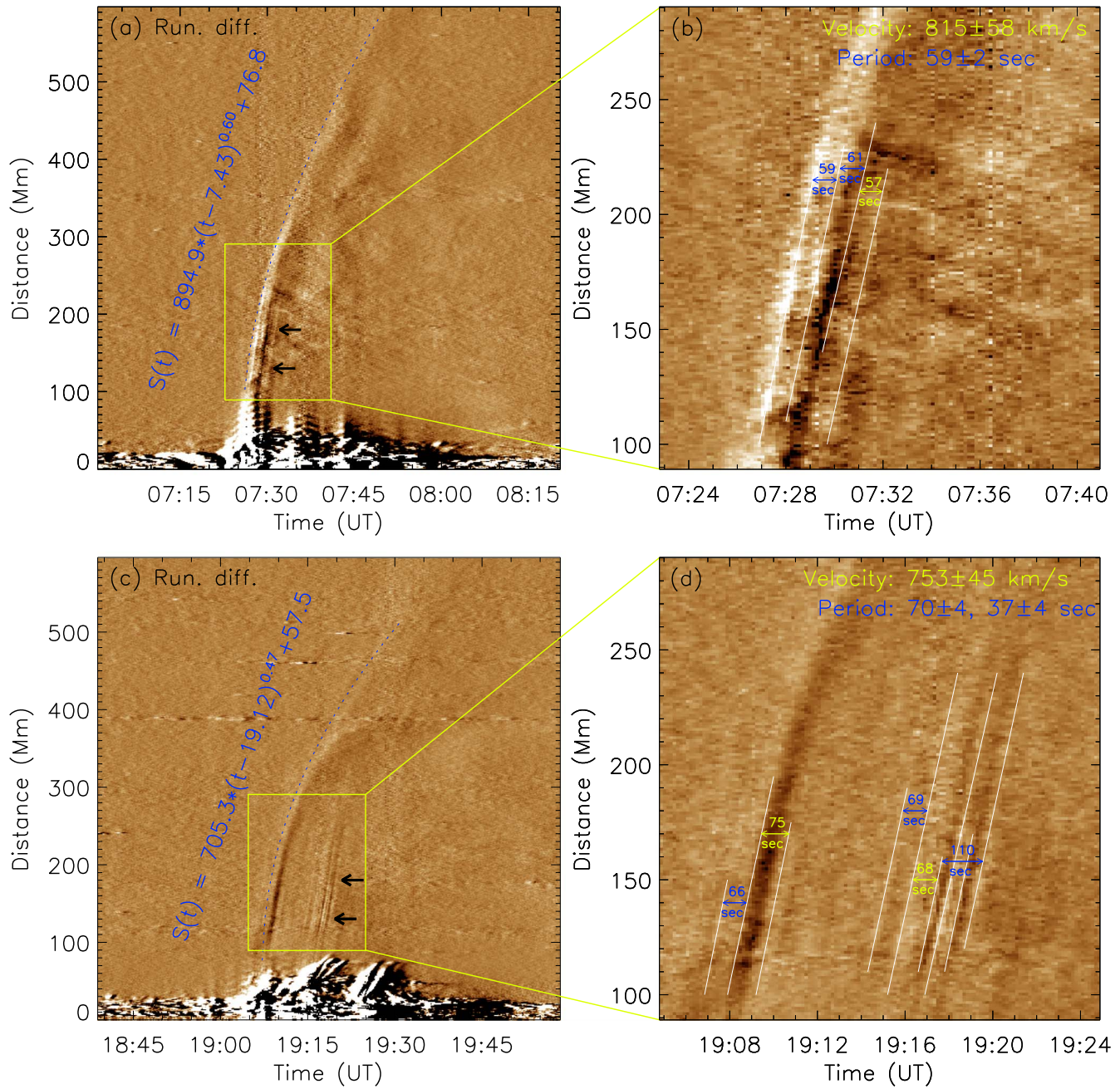


**Figure 3.** Time–distance diagrams constructed by SDO/AIA 193 Å running-difference maps. (a) Time–distance diagram along sector S1 in Figure 1(b2) for the first event. (b) The zoom-in region marked by the yellow box in panel (a). (c) Time–distance diagram along sector S2 in Figure 2(b2) for the second event. (d) The zoom-in region marked by the yellow box in panel (c). The white lines in panels (b) and (c) denote the signals of QFP wave trains.

was about  $59 \pm 2$  s. For the second QFP wave train, the signal is more distinct than the first one. Nine wave fronts could be identified in the time–distance maps, which are marked by the white lines in panel (d). According to their slope and interval, we can derive its propagating speed of about  $753 \pm 45$  km s<sup>-1</sup> and two periods of about  $70 \pm 4$  s and  $37 \pm 4$  s.

### 3.3. Variations of the Intensity Peaks of High-temperature EUV Lines in the Flare Kernel Region

To probe the excitation mechanism of QFP wave trains, we calculated the intensity peaks of EUV lines in the flare kernel region marked by the black boxes in Figures 1(b2) and 2(b2). Except for 94 and 335 Å maps recorded by SDO/AIA, other

maps of SDO/AIA EUV passbands exhibited some over-saturated emissions during the flare. Thus, to reduce the disambiguation, we only calculated the intensity peaks of 94 and 335 Å EUV lines in the flare kernel region. The intensity peak is calculated by averaging the last 20 pixels of maximum intensity in the selected region (see the black boxes in Figures 1(b2) and 2(b2)). Panels (a1) and (a2) of Figure 4 exhibit the time variations of intensity peaks of 94 and 335 Å for two QFP wave trains. To show this more visually, each sub-time–distance map of 193 Å is plotted in the upper backgrounds of each panel. One can see that some conspicuous perturbations marked by the black arrows can be identified in the intensity peak profile. These perturbations occurred in the early stage of the flare/filament eruption, which are



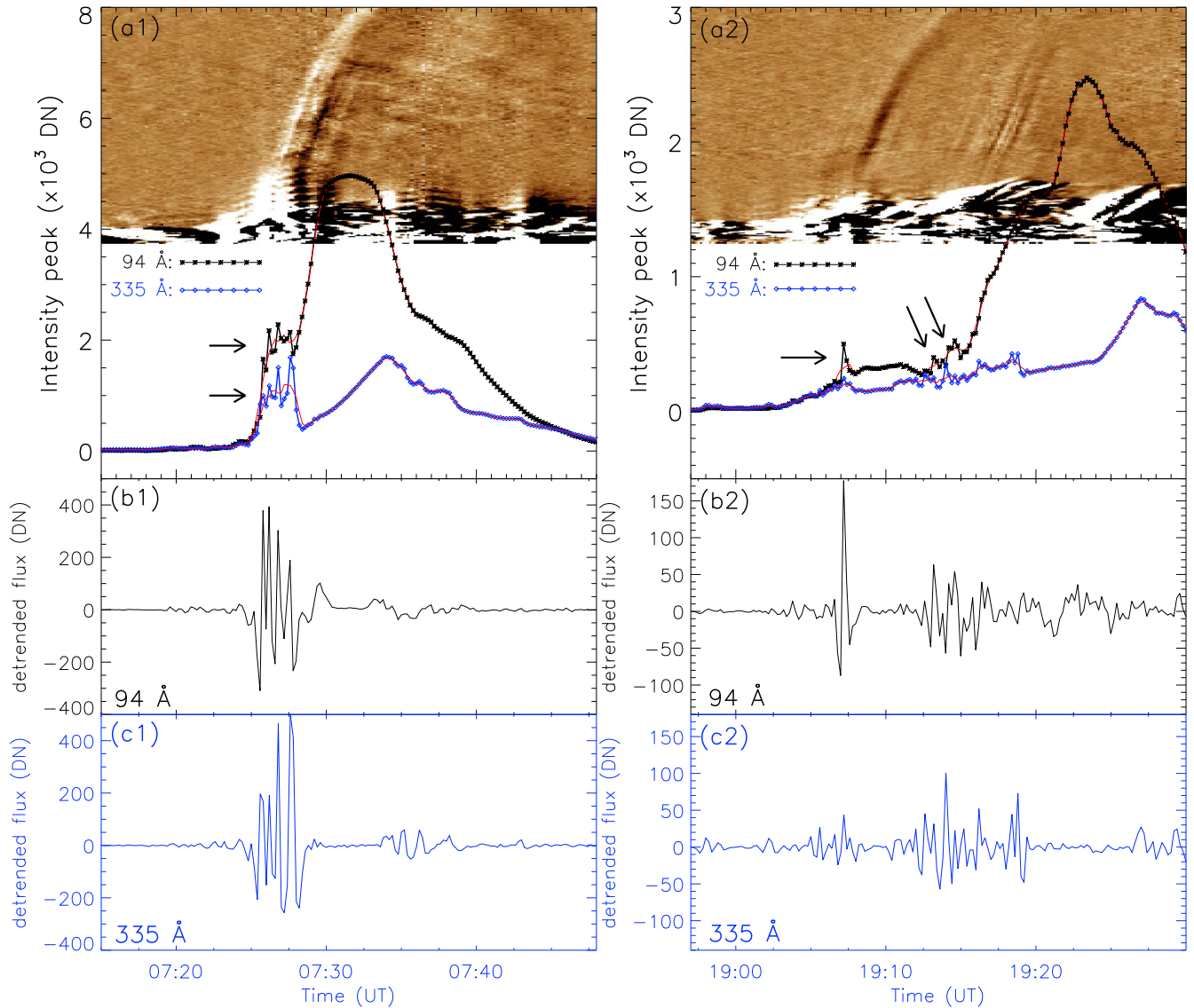


**Figure 4.** Variations of 94 and 335 Å intensity peaks in the flare kernel. (a1, a2) Profiles of intensity peaks in 94 and 335 Å passbands. The upper part is superimposed by the time–distance diagrams of the 193 Å running-difference map. The red lines are the smoothed intensity peaks using a 60 s boxcar. (b1, b2) Variations of detrended flux of 94 Å intensity peak. (c1, c2) Variations of detrended flux of 335 Å intensity peak. The detrended flux is derived by subtracting the smoothed data (see the red lines in panels (a1) and (b1)) from the original intensity. Panels (a1), (b1), and (c1) are for the first QFP wave train, while panels (a2), (b2), and (c2) are for the second QFP wave train.

contemporaneous with the reversed time in the case of the QFP wave train being excited from the flare kernel. In other words, there is a synchronization of these perturbations and the source of QFP wave trains. Therefore, these perturbations are closely related to the generation of the QFP wave trains.

Panels (b1) and (c1) plot the variations of detrended flux derived by subtracting the smoothed intensity peak using a 60 s boxcar (see the red lines in panels (a1)) from the original intensity peak of 94 and 335 Å for the first QFP wave trains, while panels (b2) and (c2) are the same but for the second QFP wave trains. Some obvious perturbations occurred in both detrended fluxes of 94 and 335 Å during occurrences of both QFP wave trains (see panels (b1) and (c1) for the first QFP wave train and panels (b2) and (c2) for the second QFP wave train). These facts guide us to suspect that the generation of QFP wave trains has a close correlation with these perturbations in the intensity peaks of high-temperature EUV lines. At least, they have a common exciting source.

By using the wavelet analysis technique (Torrence & Compo 1998), we can derive the oscillation periods in the detrended flux profiles of the 94 and 335 Å intensity peak. Figures 5(a1) and (b1) display the wavelet spectra of 94 and 335 Å detrended fluxes for the first QFP wave train, while panels (b2) and (b2) are the wavelet spectra for the second QFP wave train. For the first QFP wave train, there is a strong wavelet spectrum power during the period from 07:24 UT to 07:28 UT. This is consistent with the occurrence time of the QFP wave train. The main period of 335 Å detrended flux could be calculated to be 60 s, which is consistent with the period of the QFP wave train (see Figure 3(b)). But the main period of 94 Å detrended flux is about 36 s. It should be noted that the period of about 60 s also has a strong power in 94 Å detrended flux (see the red line in panel (a)), meaning that it is also consistent with the period of the QFP wave train. For the second QFP wave train, the strong wavelet spectrum power of both 94 and 335 Å detrended fluxes mainly occurred at around

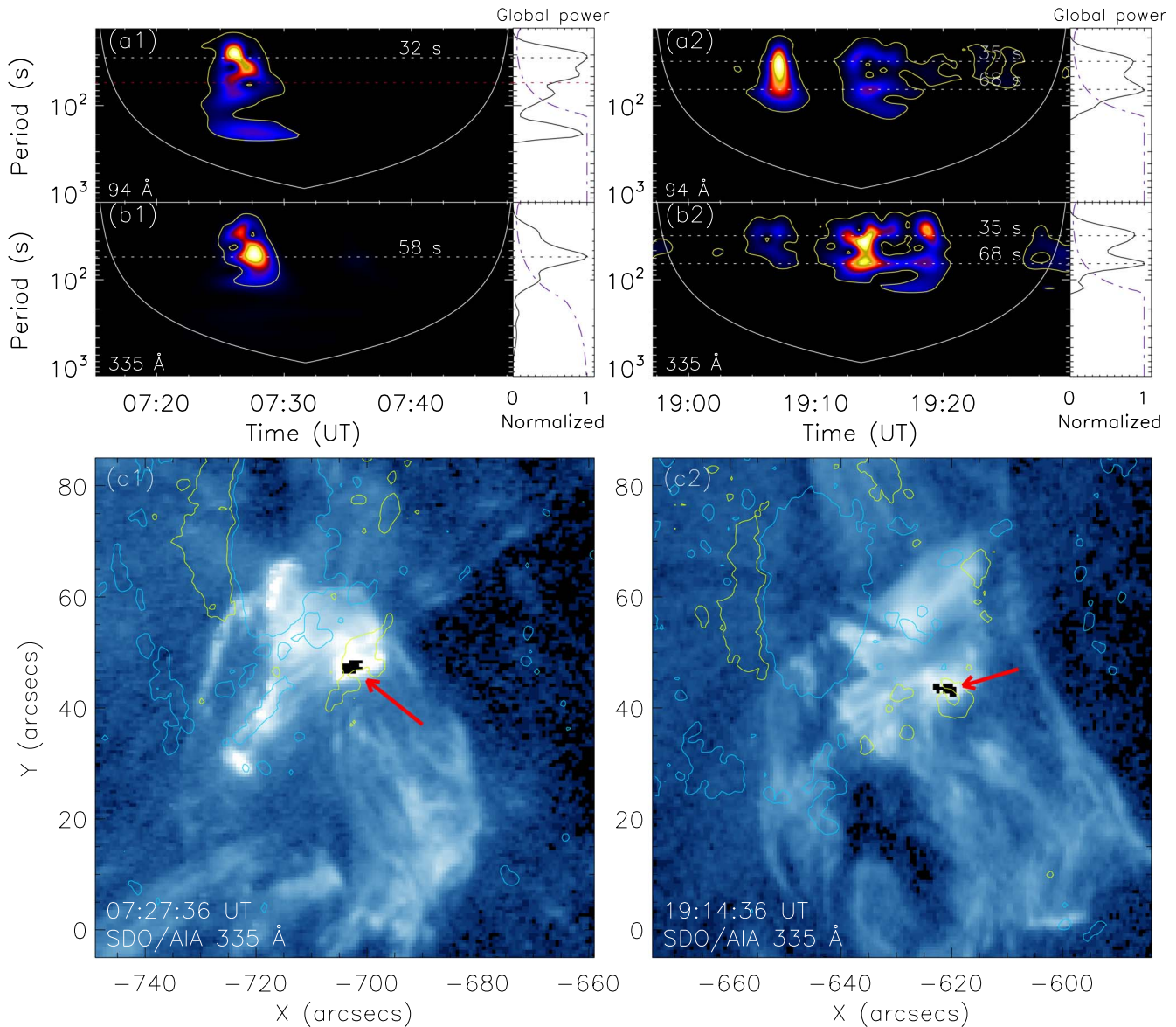


**Figure 5.** Wavelet analysis of the detrended flux of 94 and 335 Å intensity peak in the flare kernel. (a1, b1) Wavelet powers derived from the detrended flux of 94 and 335 Å intensity peaks for the first QFP wave train. (a2, b2) Wavelet powers derived from the detrended flux of 94 and 335 Å intensity peaks for the second QFP wave train. The dotted–dashed line in global power indicates the 95% significance level. (c1, c2) SDO/AIA 335 Å maps at 07:27:36 UT and 19:14:36 UT. The pixels of intensity peaks are depicted by black colors, marked by the red arrow. Yellow and blue contours are line-of-sight magnetic fields with levels of  $\pm 100$  G, respectively.

19:07 UT and 19:13 UT. This feature is consistent with the occurrence of the second QFP wave trains (see panel (d) of Figure 3). Two main periods of 36 s and 70 s could be derived in both 94 and 335 Å detrended fluxes (see panels (a2) and (b2) of Figure 5), which is also consistent with the periods of the second QFP wave trains (see panel (b) of Figure 3). All the above evidence demonstrates that the QFP wave trains have a close relationship with the perturbations in the intensity peak of high-temperature EUV lines. In other words, these two phenomena have a common excitation origin.

Figures 5(c1) and (c2) show the location of the emissions of the intensity peaks at two flaring moments for two QFP wave trains. The artificial black region marked by the red arrows indicates the location of the emissions of the intensity peak. One can see that the emissions of the intensity peak mainly originate from the one footpoint of flaring loops with positive magnetic polarities during the occurrence of the QFP wave

trains. This implies that the generation of QFP wave trains is closely associated with the downflow plasma during the flare.

#### 4. Summary and Discussion

In this letter, we present two homologous QFP wave trains induced by two small-scale filament eruptions in NOAA AR 12680 on 2017 September 12. By using the observational data from several solar telescopes, the characteristics of QFP wave trains and their closely accompanying phenomenon (the intensity peak in the flare kernel) are studied in detail. The main results are as follows:

1. Two homologous wave events including the main front CBF and the following QFP wave train, accompanied by some radio bursts and two C-class flares, were excited by two homologous small-scale filament eruptions nearby a sunspot.

2. The main CBFs propagated with the power-law functions of  $S(t) = 894.9 * (t - 7.43)^{0.60} + 76.8$  and  $S(t) = 705.3 * (t - 19.12)^{0.47} + 57.5$ , respectively. The propagating speed of the first QFP wave train was calculated to be  $815 \pm 58 \text{ km s}^{-1}$ , and the period was estimated as  $59 \pm 2 \text{ s}$ . For the second QFP wave train, its propagating speed could be derived as  $753 \pm 45 \text{ km s}^{-1}$ , and it had two periods of  $70 \pm 4 \text{ s}$  and  $37 \pm 4 \text{ s}$ .
3. The QFP wave trains are closely associated with the perturbations of 94 and 335 Å intensity peaks in the flare kernel, strongly suggesting that they have a common exciting mechanism. Furthermore, we identify that the emissions of the intensity peaks mainly originate from the one footpoint of flaring loops during the occurrences of QFP wave trains.

The ambient condition has a significant effect on the propagation of a coronal MHD shock wave. Many observational CBF events have been excited by some eruptions nearby a sunspot (e.g., Liu et al. 2010; Chen & Wu 2011; Xue et al. 2013; Zhang et al. 2015). Wang et al. (2020) proposed that the eruption beside the sunspot would be favorable for the discovery of different perturbations (such as CBFs and Moreton–Ramsey waves) in the solar atmosphere. These two homologous wave events were also excited by the small-scale filament eruptions near a sunspot. These facts demonstrate that the eruptions beside the footpoint of concentrated large-scale loops easily induce the large-scale CBFs. In other words, a funnel coronal loop system may set a favorable condition for the propagation of the different large-scale global perturbations (Roberts et al. 1983).

We found that the traveling paths of the main CBFs ahead of the QFP wave trains are subject to the power-law function, which indicates that the main CBFs propagate on a decelerating pattern with a decreasing rate. This is consistent with previous studies (e.g., Warmuth et al. 2005; Veronig et al. 2008; Wang et al. 2020), which can be explained by the propagation of a nonlinear fast-mode shock wave whose propagation speed in a homogeneous and isotropic environment theoretically depends on the Mach number or wave amplitude (Vršnak et al. 2016). These two main CBFs are also obviously induced by two homologous small-scale filament eruptions. In general, these CBFs have been proposed to be excited by the associated flares (Vršnak & Cliver 2008) or driven by the CMEs (Biesecker et al. 2002; Nitta et al. 2013; Muhr et al. 2014). Based on the fact of the synchronization of the CME acceleration phase and the impulsive phase of the associated flare, it is hard to determine which process is dominant. In our two events, they also generated two narrow CMEs, whose acceleration phases started at around 07:25 UT and 19:13 UT according to the Solar Terrestrial Relations Observatory (STEREO) observation. Figures 3(b) and (d) show that the first appearances of these two main CBFs at 100 Mm away from the source region are at around 07:27 UT and 19:08 UT, respectively. It is found that the first main CBF occurred behind the CME acceleration phase while the second occurred in front of the CME acceleration phase. This suggests that the second main CBF was not triggered by the CME. On the other hand, the traveling profiles of these two main CBFs are very similar to those of the QFP wave trains during the occurrences of the QFP wave trains, or the main CBF can be regarded as one wave front of QFP wave trains (see Figures 3(a) and (c)), which suggests that they have a common trigger mechanism. Therefore, we propose

that these two main CBFs should also be excited by the associated flare.

The periods of QFP wave trains have been obtained in the range from seconds to a few minutes (Liu et al. 2011, 2012; Shen & Liu 2012). We also find that the periods of QFP wave trains in our study are about 40, 60, and 70 s, which is consistent with previous studies. On the other hand, these QFP wave trains almost traveled with a constant projected velocity of about  $800 \text{ km s}^{-1}$  along the path on the solar surface, which is well within the Alfvén (fast) wave speed range in the coronal condition (about  $735\text{--}845 \text{ km s}^{-1}$ ; Yuan et al. 2013).

The exciting mechanism of QFP wave trains is the main subject in the studies of the QFP wave trains. These two homologous QFP wave trains in our study have a tempestuous relationship with the perturbations in intensity peak of 94 and 335 Å passband in the flare kernel, suggesting that they have a common excitation origin, which further strongly demonstrates that they are excited by the energy release associated with magnetic reconnection instead of by the dispersion evolution of the broad propagating magnetosonic waves. This result is consistent with previous studies (Liu et al. 2010, 2012; Shen & Liu 2012). Another, more intriguing finding in our study is that the intensity peak of 94 and 335 Å mainly originated from the one footpoint of flare loops during the appearance of the QFP wave trains. This fact implies that the emissions at the footpoint of flaring loops are also modulated by the origin of the QFP wave trains. There may be two possibilities for this implication. One possibility is that the QFP wave trains are directly excited by the discontinuous downflow plasma along the flaring loop after the discontinuous magnetic reconnection. In this case, discontinuous outflows from the intermittent magnetic reconnection bombard the dense solar atmosphere along the flare loop, which would result in QFP wave trains and the perturbations in the emissions of the intensity peak. Another possibility is that the QFP wave trains are spontaneously excited by the above-the-loop-top oscillation provoked by the outflow in a quasi-steady magnetic reconnection (Takasao & Shibata 2016). In this situation, the oscillation of the arms of the magnetic tuning fork driven by the interaction between the backflow and magnetic fields in the above-the-loop-top region causes the generation of the quasi-periodical outward-propagating fast waves that evolve to be observed QFP wave trains. Due to the influence of above-the-loop-top oscillation, downflow plasma along the flaring loop would exhibit a quasi-periodical pattern during the occurrence of QFP wave trains. The emissions at the footpoint of flaring loops should respond to the variation of this discontinuous downflow plasma. Therefore, the emission at the footpoint shows some turbulence during the QFP wave trains. Furthermore, Ning (2017) suggested that the 1-minute QFPs originate from the footpoints of the flare loops. And Takasao & Shibata (2016) suggested that QFP wave trains and QFPs in the nonthermal emissions may have a common origin. Thus, it seems plausible that the emissions at the flare loop footpoints and the QFP wave trains are tightly related phenomena.

We appreciate the referee’s careful reading of the manuscript and many constructive comments, which helped greatly in improving the paper. SDO is a mission of NASA’s Living With a Star Program. The authors are indebted to the SDO, GONG, GOES, Wind, and NVST teams for providing the data. This work is supported by the National Science Foundation of China



(NSFC) under grant Nos. 12003064, 11873087, 11803085, and 11973084; the Yunnan Key Laboratory of Solar Physics and Space Science (202205AG070009); the National Key R&D Program of China (2019YFA0405000); the Yunnan Science Foundation of China (2019FD085, 202101AT070032, 202201AT070194); Youth Innovation Promotion Association, CAS (No. 2019061) and Yunnan Science Foundation for Distinguished Young Scholars No. 202001AV070004, the grant associated with a project of the Group for Innovation of Yunnan province.

### ORCID iDs

Jincheng Wang  <https://orcid.org/0000-0003-4393-9731>  
 Xiaoli Yan  <https://orcid.org/0000-0003-2891-6267>  
 Zhike Xue  <https://orcid.org/0000-0002-6526-5363>  
 Liheng Yang  <https://orcid.org/0000-0003-0236-2243>  
 Qiaoling Li  <https://orcid.org/0000-0003-2045-8994>  
 Zhe Xu  <https://orcid.org/0000-0002-9121-9686>

### References

- Antiochos, S. K., DeVore, C. R., & Klimchuk, J. A. 1999, *ApJ*, 510, 485  
 Bi, Y., Jiang, Y., Yang, J., et al. 2016, *NatCo*, 7, 13798  
 Biesecker, D. A., Myers, D. C., Thompson, B. J., et al. 2002, *ApJ*, 569, 1009  
 Bougeret, J.-L., Kaiser, M. L., Kellogg, P. J., et al. 1995, *SSRv*, 71, 231  
 Cabezas, D. P., Asai, A., Ichimoto, K., et al. 2019, *ApJ*, 883, 32  
 Chen, P. F., Wu, S. T., Shibata, K., et al. 2002, *ApJL*, 572, L99  
 Chen, P. F., & Wu, Y. 2011, *ApJL*, 732, L20  
 Duan, Y., Shen, Y., Zhou, X., et al. 2022, *ApJL*, 926, L39  
 Gilbert, H. R., Holzer, T. E., Burkepile, J. T., et al. 2000, *ApJ*, 537, 503  
 Harvey, J. W., Hill, F., Hubbard, R. P., et al. 1996, *Sci*, 272, 1284  
 Hoeksema, J. T., Liu, Y., Hayashi, K., et al. 2014, *SoPh*, 289, 3483  
 Kozarev, K. A., Korreck, K. E., Lobzin, V. V., et al. 2011, *ApJL*, 733, L25  
 Lemen, J. R., Title, A. M., Akin, D. J., et al. 2012, *SoPh*, 275, 17  
 Li, B., Antolin, P., Guo, M.-Z., et al. 2020, *SSRv*, 216, 136  
 Li, D., Ge, M., Dominique, M., et al. 2021, *ApJ*, 921, 179  
 Li, D., & Yao, S. 2020, *ApJ*, 891, 79  
 Lin, J., & Forbes, T. G. 2000, *JGR*, 105, 2375  
 Liu, W., Nitta, N. V., Schrijver, C. J., et al. 2010, *ApJL*, 723, L53  
 Liu, W., & Ofman, L. 2014, *SoPh*, 289, 3233  
 Liu, W., Ofman, L., Nitta, N. V., et al. 2012, *ApJ*, 753, 52  
 Liu, W., Title, A. M., Zhao, J., et al. 2011, *ApJL*, 736, L13  
 Liu, Z., Xu, J., Gu, B.-Z., et al. 2014, *RAA*, 14, 705  
 Miao, Y., Li, D., Yuan, D., et al. 2021, *ApJL*, 908, L37  
 Moreton, G. E. 1960, *AJ*, 65, 494  
 Moreton, G. E., & Ramsey, H. E. 1960, *PASP*, 72, 357  
 Muhr, N., Veronig, A. M., Kienreich, I. W., et al. 2014, *SoPh*, 289, 4563  
 Munro, R. H., Gosling, J. T., Hildner, E., et al. 1979, *SoPh*, 61, 201  
 Nakariakov, V. M., & Verwichte, E. 2005, *LRSP*, 2, 3  
 Ning, Z. 2014, *SoPh*, 289, 1239  
 Ning, Z. 2017, *SoPh*, 292, 11  
 Ning, Z., Wang, Y., Hong, Z., et al. 2022, *SoPh*, 297, 2  
 Nisticò, G., Pascoe, D. J., & Nakariakov, V. M. 2014, *A&A*, 569, A12  
 Nitta, N. V., Schrijver, C. J., Title, A. M., et al. 2013, *ApJ*, 776, 58  
 Ofman, L., & Thompson, B. J. 2002, *ApJ*, 574, 440  
 Pascoe, D. J., Nakariakov, V. M., & Kupriyanova, E. G. 2013, *A&A*, 560, A97  
 Pesnell, W. D., Thompson, B. J., & Chamberlin, P. C. 2012, *SoPh*, 275, 3  
 Reinard, A. A., & Biesecker, D. A. 2008, *ApJ*, 674, 576  
 Reiner, M. J., Kaiser, M. L., & Bougeret, J.-L. 2007, *ApJ*, 663, 1369  
 Roberts, B., Edwin, P. M., & Benz, A. O. 1983, *Natur*, 305, 688  
 Schmieder, B., Aulanier, G., & Vršnak, B. 2015, *SoPh*, 290, 3457  
 Shen, Y., & Liu, Y. 2012, *ApJ*, 753, 53  
 Shen, Y., Zhou, X., Duan, Y., et al. 2022, *SoPh*, 297, 20  
 Takasao, S., & Shibata, K. 2016, *ApJ*, 823, 150  
 Tan, B., Zhang, Y., Tan, C., et al. 2010, *ApJ*, 723, 25  
 Torrence, C., & Compo, G. P. 1998, *BAMS*, 79, 61  
 Uchida, Y. 1968, *SoPh*, 4, 30  
 Veronig, A. M., Temmer, M., & Vršnak, B. 2008, *ApJL*, 681, L113  
 Vršnak, B., & Cliver, E. W. 2008, *SoPh*, 253, 215  
 Vršnak, B., Žic, T., Lulić, S., et al. 2016, *SoPh*, 291, 89  
 Wang, J., Yan, X., Kong, D., et al. 2020, *ApJ*, 894, 30  
 Wang, J., Yan, X., Qu, Z., et al. 2017, *ApJ*, 839, 128  
 Warmuth, A. 2015, *LRSP*, 12, 3  
 Warmuth, A., & Mann, G. 2011, *A&A*, 532, A151  
 Warmuth, A., Mann, G., & Aurass, H. 2005, *ApJL*, 626, L121  
 Xu, Z., Yang, J., Ji, K., et al. 2019, *ApJ*, 874, 134  
 Xue, Z., Yan, X., Cheng, X., et al. 2016, *NatCo*, 7, 11837  
 Xue, Z. K., Qu, Z. Q., Yan, X. L., et al. 2013, *A&A*, 556, A152  
 Yan, X., Liu, Z., Zhang, J., & Xu, Z. 2020, *ScChE*, 63, 1656  
 Yan, X., Xue, Z., Jiang, C., et al. 2022, *NatCo*, 13, 640  
 Yan, X. L., Wang, J. C., Pan, G. M., et al. 2018, *ApJ*, 856, 79  
 Yokoyama, T., & Shibata, K. 1995, *Natur*, 375, 42  
 Yuan, D., Shen, Y., Liu, Y., et al. 2013, *A&A*, 554, A144  
 Zhang, Y., Zhang, J., Wang, J., et al. 2015, *A&A*, 581, A78  
 Zhou, X., Shen, Y., Su, J., et al. 2021, *SoPh*, 296, 169